Journal of Energy Storage 93 (2024) 112230

Contents lists available at ScienceDirect

Journal of Energy Storage

journal homepage: www.elsevier.com/locate/est

Research papers

Non-dimensional numerical analysis of coupled Metal Hydride-Phase Change Material hydrogen storage system

Marco Maggini [a], Giacomo Falcucci [b,c], Alessandro Rosati [a,d], Stefano Ubertini [a], Andrea L. Facci [a,*]

[a] Department of Economics, Engineering, Society and Business Organization, University of Tuscia, 01100 Viterbo, Italy
[b] Department of Enterprise Engineering Mario Lucertini, University of Rome Tor Vergata, Via del Politecnico 1, 00133 Rome, Italy
[c] Department of Physics, Harvard University, Cambridge, MA 02138, USA
[d] AzzeroCO2 s.r.l., Via Genova 23, 00184 Rome, Italy

ARTICLE INFO

Dataset link: https://github.com/marco-maggini/Paper-Metal-Hydride-non-dimensional-Analysis---Main-Code.git

Keywords:
Energy storage
Hydrogen storage
Metal hydride
Phase change material

ABSTRACT

Efficient storage solutions that decouple energy use and production are pivotal for the green energy transition, due to the non-controllable operation of solar and wind power. In this scenario, hydrogen, and in particular metal hydride storage, has shown excellent potential.

In this paper we develop a mathematical model to characterize the operation of several cylindrical Metal Hydride-Phase Change Material tank layouts and to determine the improved configuration in terms of charge/discharge time and power. We use non-dimensional parameters to guide the design of a hybrid metal hydride-phase change material hydrogen storage system. We introduce a critical value for the state of charge of the storage system, equal to $\phi_c^* = 0.15$, above which heat exchange dominates the process efficiency. Results show that, when varying the canister main aspect ratio between 5 and 100, the equivalent inlet/outlet power increases by a factor ≈ 10. The ratio of the thermal conductivities is found to have a significant impact in the desorption phase, where the equivalent power increases by a factor ≈ 4 when raising the ratio from 0.1 to 0.8.

Finally, we evaluate three case studies by introducing three different improved configurations and comparing them with the baseline design. A $LaNi_5/LiNO_3 - 3H_2O$ system for the storage of 1 kWh of H_2 exhibits 5.65 kW and 0.83 kW of average power in absorption and desorption, respectively. Such an improved configuration is 93% faster in charge/discharge process with respect to the baseline design. A coupled Mg_2NiH_4 - $NaNO_3$ exhibits 2.93 kW and 0.30 kW of average power in absorption and desorption, respectively. This configuration is 81% faster than the baseline design. A coupled Mg_2NiH_4 - KNO_3 exhibits 1.66 kW and 0.56 kW of average power in absorption and desorption, while the cycle time is reduced from 1220 min to 147 min (−88%).

1. Introduction

The transition from fossil fuels to Renewable Energy Sources (RES) is crucial to achieving the ambitious climate energy objectives set by the European Commission Energy Roadmap 2050 [1] and the 17 Sustainable Development Goals of the United Nations [2]. The implementation of RES (mainly solar and wind power) within the existing grid has already been partially accomplished, but their intermittent nature lays several challenges for their large-scale integration [3]. In fact, their variability as a function of weather and time conditions causes significant problems to the stability and the operation of the power system [4]. To maximize the flexibility of the entire energy system and to reach low-carbon energy goals, the following achievements are pivotal: (i) the massive spread of smart grids, able to handle bidirectional electrical flows in an optimized way [5]; (ii) the intelligent exploitation of carbon neutral energy carriers (e.g., hydrogen); (iii) the large scale implementation of secure, effective, and efficient energy storage systems [6], capable of solving the temporal mismatch between production and use of RES.

In this wide and complex context, hydrogen has shown excellent potential as energy carrier [7] and as energy storage medium [8]. In fact, it can provide potentially carbon neutral, clean and secure energy to all sectors of the economy, including hard-to-abate ones (industry, transportation and buildings) [9–12]. Such an extensive utilization of hydrogen needs harmless, compact, light, and cost-efficient hydrogen

* Corresponding author.
E-mail address: andrea.facci@unitus.it (A.L. Facci).

https://doi.org/10.1016/j.est.2024.112230
Received 8 February 2024; Received in revised form 20 May 2024; Accepted 22 May 2024
Available online 30 May 2024

Nomenclature

D	Canister diameter
V	Canister volume
$\mathcal{L}$	Canister length
S	Inlet valve surface area
ξ	Hydride porosity
b	Canister radius
C	Kinetic constant
ΔH	Enthalpy variation
ΔS	Entropy variation
E	Activation energy
Fo	Fourier number
M	Metal Hydride molecular weight
Nu	Nusselt number
P	Equivalent Power
Pr	Prandtl number
Ra	Rayleigh number
S_c	Stoichiometric Coefficient
T	Temperature
c_p	Specific heat
f	Hydrogen mass flow rate
h	Convective heat exchange coefficient
k	Thermal conductivity
m	Mass
p	Pressure
$\dot{q}$	Volumetric heat source term
r	Reaction rate
t	Time

Abbreviations

MF	Metal Foam
MH	Metal Hydride
PCM	Phase Change Material
RES	Renewable Energy Sources

Greek Letters

α	Thermal diffusivity
β	Reaction plateau slope coefficient
λ	Latent heat of fusion
μ	Viscosity
ϕ	State of charge
ρ	Density

Subscripts

a	Absorption
d	Desorption
e	Effective
env	Environment
eq	Equilibrium
in	Inlet
l	Liquid
m	Metal powder
out	Outlet
s	Solid

storage [13]. The main hydrogen storage methods include gas, liquid, and solid storage [14].

Among these methods, solid state Metal Hydride (MH) hydrogen storage is one of the most promising solutions for both stationary and mobile applications [15]. Compared to other storage technologies, MHs are safer and more reliable, have a higher hydrogen volumetric density, comparatively low operating pressure, and can operate at room temperature [16,17]. Nonetheless, none of the current MH technologies fulfills all the essential criteria for a practical hydrogen economy [18], primarily due to their slow kinetics and the challenges associated with controlling MH temperatures during hydrogen absorption and release. Advanced thermal control and management are crucial to enhance MH performance [19–21]. Literature shows significant research and development efforts to improve heat transfer in the MH tanks, in order to efficiently operate alternate heating and cooling and obtain reaction times of practical interest. In particular, current research focuses on: (i) techniques to improve the effective thermal conductivity of the MH bed; (ii) design of high-efficiency internal/external heat exchangers; (iii) Phase Change Materials (PCMs) utilization.

Several studies focus on the usage of heat exchangers such as straight tubes [22], helically coiled tubes [23], multi-tubes [24], tubes with fins [25,26], and heat pipes [27] to generate the desorption heat or extract the absorption heat. Such solutions effectively improve reaction kinetics but they require an external energy source and an active control system.

A more effective and efficient solution is storing the heat emitted by the MH during the absorption process and then to reuse it in the desorption process. Such a regenerative process can be achieved through the thermal coupling of MH with phase change materials that store and release heat in a narrow temperature range through melting and solidification [28]. Currently, various studies investigate different aspects of MH-PCM coupling. Garrier et al. [29] coupled a MgH_2 MH tank with a metallic alloy PCM based on Mg–Zn eutectic. They designed and tested a tank of 7000 NL of hydrogen (21 kWh) and demonstrated a storage efficiency of around 70%. They also provided an estimate of the impact of the PCM thermal conductivity on the global reactor performance. Darzi et al. [30] numerically investigated a $LaNi_5$ tank coupled with a Rubitherm-based PCM. The authors separately assess the influence of the charge, discharge pressure, the MH bed porosity, and the PCM's thermal conductivity. Nyamsi et al. [31] numerically investigate the behavior of a hybrid $LaNi_5$ - Paraffin PCM finned jacket. The impact of PCM thermal conductivity, latent heat, density, heat capacity, melting point, as well as fins geometry, is evaluated in a multi-objective optimization with the aim to reduce charge and discharge time. The authors find an optimal configuration which reduces ab/desorption time of 49% and 4%. Amati et al. [32] employed a three-phase Lattice Boltzmann model to evaluate the performance of PCM-based latent heat thermal energy storage systems. The authors compare the effectiveness of different thermal conductivity enhancement supports, i.e., fins, blades, and novel branched fractal structures. They demonstrate the superiority of the latter option in terms of cycle time reduction.

The choice of an appropriate PCM and the optimization of its quantity are essential to ensure efficient heat transfer and fast hydrogen charge and discharge rates [21,33,34]. The PCM should have high thermal conductivity and melting enthalpy and a suited phase change temperature. In [35], the authors examine a MH-PCM system studying the PCM choice and evaluating the effect of several thermodynamic properties such as melting temperature, latent heat of fusion, specific heat capacity, density, and thermal conductivity. Particularly, the thermal conductivity parameter is low for most PCMs [36] and an improvement is needed to enhance the heat exchange. In this perspective, Metal Foam (MF) can be integrated into both the PCM and the MH. Various studies have investigated the integration of different MFs into the metal hydride to improve the hydrogen storage performance [37,38], and into PCM to improve thermal storage performance [39–41].

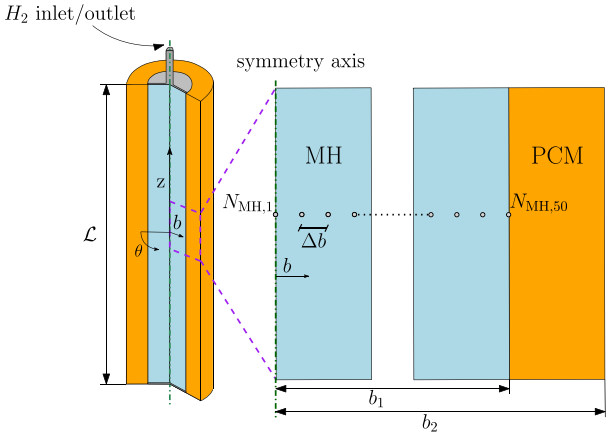

Fig. 1. The MH-PCM system configuration and domain discretization [from b_0 (vessel core) to b_1 (MH-PCM interface).].

The studies hereby revised focus on the design and performance optimization of specific configurations of the MH-PCM integrated canisters, on the optimization of pre-arranged layouts, or on the impact of individual thermo-physical parameters on the storage performance. They all apply the heat and mass transfer governing equations to a limited number of selected arrangements. Conversely, to the best of our knowledge, a general analysis of the impact of the relevant parameters on the system performance, able to guide the canister initial design process is still untapped. To this aim, in this paper, we utilize dimensional analysis to determine the most influential parameters, to analyze their effects on the system performance and guide through the preliminary design of different cylindrical MH-PCM tank layouts. In particular, by using the Buckingham theorem we combine the geometrical and physical properties of PCM and MH to obtain non-dimensional numbers representative of the problem.

The paper is organized as follows. In Section 2 we describe the system, the mathematical model, the domains discretization, the heat exchange model, the problem non-dimensionalization, and the model validation. Results for the absorption and desorption processes are presented and discussed in Section 3. In Section 4 we highlight the main aspects of the results. Moreover, we introduce three case studies to assess the usefulness of the methodology. Finally, we draw the conclusions in Section 5.

2. Methodology

2.1. System description

The system is made of an inner MH cylinder of length $\mathcal{L}$, radius b_1, diameter D, and porosity $\xi = 0.5$ (see, for instance, [42]) surrounded by a hollow PCM cylinder of radius b_2, as shown in Fig. 1. Without loosing generality, we assume that the system is thermally insulated (see [43]) and that $\mathcal{L} \gg b_1$. Hydrogen flows to/from the MH canister through a 5 mm diameter valve. In the following calculations, we use a cylindrical coordinate system (see Fig. 1) with the z-axis along the canister length.

A complete cycle consists of charge, dormancy, and discharge phases (see Fig. 2).

The PCM serves as heat storage to passively control the MH temperature. Its melting/solidification temperature matches the MH equilibrium temperature at the selected storage pressure. Therefore, during the charging phase, the hydrogenation heat flows from the MH to the PCM that melts at (almost) constant temperature. In this phase H_2 is provided to the system at a pressure p_{in}, higher than the equilibrium pressure (p_{eq}). Hydrogen enters the inner cylinder and is absorbed in the MH bed. In the dormancy phase, MH continues heating the PCM

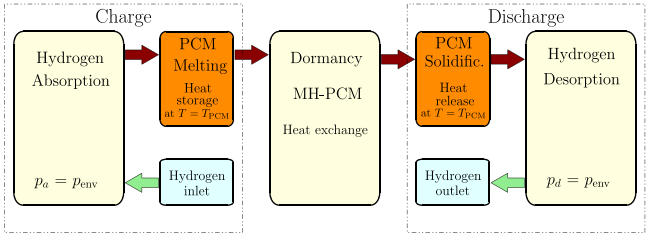

Fig. 2. The whole process in the MH-PCM storage system.

until a steady-state condition is reached (i.e., when the hydride has the same temperature of the PCM). Conversely, during dehydrogenation, the PCM heats the MH using the thermal energy stored during hydrogenation. In this phase p_{out} is lower than p_{eq}.

2.2. Mathematical modeling

The mathematical model is built under the following hypotheses: (i) all gases are ideal and the flow compressible (see for instance [44]); (ii) the porous medium is homogeneous (see for instance [45]); (iii) both inlet/outlet hydrogen pressures are constant (see for instance [46]); (iv) the physical properties of MH/PCM are not functions of their temperature [47]; (v) the gas pressure inside the vessel is uniform therefore no momentum conservation is accounted for [44]; (vi) the gas and the MH are locally in thermal equilibrium.

2.2.1. MH modeling

We discard all the irreversibilities which lower the system efficiency, such as the metal powder pulverization and self-densification [48] and we model the MH reversible dynamics through mass and energy conservation equations [49]. Mass conservation reads:

$$\frac{\mathrm{d}m_{\mathrm{H_{2g}}}}{\mathrm{dt}} = f_{\mathrm{H_2}} - r m_t \frac{M_{\mathrm{H_2}} S_c}{M_{\mathrm{MH}}}, \tag{1}$$

where $m_{\mathrm{H_{2g}}}$ is the gaseous H_2 in the canister, $f_{\mathrm{H_2}}$ is its mass flow rate (positive during charge and negative during discharge), and $r = \frac{1}{m_t}\frac{\mathrm{d}m_{\mathrm{MH}}}{\mathrm{dt}}$ is the reaction rate, being m_{MH} the hydrogenated metal mass and m_t the total hydride mass. Finally, $M_{\mathrm{H_2}}$ and M_{MH} are the hydrogen and MH molecular weights and S_c is the reaction stoichiometric coefficient.

The inlet/outlet hydrogen mass flow rate is:

$$f_{H_2} = \rho_c S \sqrt{\gamma R_{H_2} T_c}, \tag{2}$$

when the flow is choked, or:

$$f_{H_2} = \frac{S}{R_{H_2} T_{in}} \sigma \sqrt{\frac{2\gamma}{\gamma} R_{H_2} T_{in} \left(1 - \delta^{\frac{\gamma-1}{\gamma}}\right)}, \tag{3}$$

otherwise. ρ_c and T_c are the hydrogen critic density and temperature, respectively. S is the inlet valve surface area, γ is the heat capacity ratio, R_{H_2} is the hydrogen gas constant, T_{in} is the inlet hydrogen temperature, $\sigma = p_{in}^{\frac{\gamma-1}{\gamma}} p^{\frac{1}{\gamma}}$ in absorption and $\sigma = p^{\frac{\gamma-1}{\gamma}} p_{out}^{\frac{1}{\gamma}}$ in desorption, $\delta = \frac{p}{p_{in}}$ in absorption and $\delta = \frac{p_{out}}{p}$ in desorption.

In absorption, the reaction rate is calculated as:

$$r = C_a e^{-\frac{E_a}{RT}} \ln \frac{p}{p_{eq}} \left(1 - \frac{m_{\mathrm{MH}}}{m_t}\right), \tag{4}$$

where C_a is the absorption kinetic constant, E_a is the absorption activation energy, R is the universal gas constant, T is the local temperature, and $p = \frac{m_{\mathrm{H_{2g}}} RT}{M_{\mathrm{H_2}} V}$ is the hydrogen pressure (V is the canister volume). In desorption:

$$r = C_d e^{-\frac{E_d}{RT}} \frac{p - p_{eq}}{p_{eq}} \left(\frac{m_{\mathrm{MH}}}{m_t}\right), \tag{5}$$

where C_d is the desorption kinetic constant, and E_d is the desorption activation energy.

In turn, the equilibrium pressure p_{eq} reads:

$$p_{eq} = p_0\, e^{\left[\frac{\Delta H}{RT} - \frac{\Delta S}{R} + \beta\left(\frac{m_{\mathrm{MH}}}{m_t} - \frac{1}{2}\right)\right]}, \tag{6}$$

where $p_0 = 1\,\mathrm{bar}$ is the reference pressure, ΔH and ΔS are the enthalpy/entropy variations, and β is the reaction plateau slope coefficient.

Eq. (7) represents the energy conservation:

$$(\rho c_p)_e \frac{\partial T}{\partial t} = k_e \nabla^2 T + \dot{q}, \tag{7}$$

being k_e the effective thermal conductivity , $(\rho c_p)_e$ the effective heat capacity, and $\dot{q}$ the volumetric heat source. In turn, k_e and $(\rho c_p)_e$ are calculated as [43,50]:

$$k_e = \xi k_{\mathrm{H_2}} + (1-\xi) k_{\mathrm{m}}, \tag{8a}$$

$$(\rho c_p)_e = \xi \rho_{\mathrm{H_2}} c_{p\mathrm{H_2}} + (1-\xi)\rho_{\mathrm{m}} c_{p,\mathrm{m}}, \tag{8b}$$

where $k_{\mathrm{H_2}}$, $\rho_{\mathrm{H_2}}$, $c_{p\mathrm{H_2}}$ are the hydrogen conductivity, density, and specific heat, respectively, and k_{m}, ρ_{m}, and $c_{p\mathrm{m}}$ are the MH conductivity, density, and specific heat. The heat source is:

$$\dot{q} = -\Delta H r(\xi \rho_{\mathrm{MH}}) \frac{S_c}{M_{\mathrm{MH}}}. \tag{9}$$

Note that ΔH is negative in absorption and positive in desorption.

Notably, during dormancy, no reactions occur, the energy conservation is the only active equation, and $\frac{dm_{\mathrm{H_2}}}{dt} = 0$. During this phase, heat is still exchanged between the two materials and the temperatures slowly converge to a steady-state condition.

2.2.2. PCM modeling

During the discharging phase, conduction is the leading heat exchange mechanism [50]. To solve the classic Stefan problem, we model the PCM solidification through the Fourier energy equation (Eq. (10)) and liquid/solid interface position (Eq. (11)) [51]:

$$\frac{\partial T_s}{\partial t} = \alpha_{\mathrm{PCM,s}} \nabla^2 T_s, \tag{10a}$$

$$\frac{\partial T_l}{\partial t} = \alpha_{\mathrm{PCM,l}} \nabla^2 T_l, \tag{10b}$$

$$\frac{\mathrm{d}\epsilon}{\mathrm{dt}} = \frac{1}{\rho_{\mathrm{PCM}} \lambda}\left[k_{\mathrm{PCM},s} \frac{\partial T_s}{\partial b}_{b=\epsilon} - k_{\mathrm{PCM},l} \frac{\partial T_l}{\partial b}_{b=\epsilon}\right]. \tag{11}$$

In Eq. (10), α_{PCM} is the PCM thermal diffusivity. In Eq. (11) ϵ is the solid/liquid interface position, ρ_{PCM} is the PCM density, λ is the PCM latent heat of fusion, and k_{PCM} is the PCM conductivity. Finally, s and l subscripts indicate solid and liquid regions, respectively.

Conversely, during absorption and dormancy, the convection dominates the heat exchange within the PCM. Therefore, we model the PCM melting through a lumped parameter model where:

$$\dot{\mathrm{Q}} = \frac{\mathrm{Nu}\, k_{\mathrm{PCM}}}{\mathcal{L}} A\,(T_{\mathrm{surf}} - T_{\mathrm{PCM}}), \tag{12}$$

where $\dot{\mathrm{Q}}$ is the thermal power, Nu is the Nusselt number, $A = 2\pi b_1 \mathcal{L}$ is the heat exchange surface area, T_{surf} is the temperature at the MH/PCM interface, and T_{PCM} is the PCM melting temperature.

In turn, following [52] Nusselt number reads:

$$\mathrm{Nu} = \frac{0.35\mathrm{Ra}^{0.25}}{[1 + (0.143/\mathrm{Pr})^{9/16}]^{4/9}}, \tag{13}$$

where Ra is the Rayleigh number and Pr is the Prandtl number. Notably, following [19] we have assumed the steady state value for Nu, discarding dynamic effects that are significant only in the very first stages of the melting process.

The mass of the PCM is selected on the basis of the reaction enthalpy:

$$m_{\mathrm{PCM}} = \frac{\%wt \cdot m_t \cdot \frac{\Delta H}{M_{\mathrm{H_2}}}}{\lambda}, \tag{14}$$

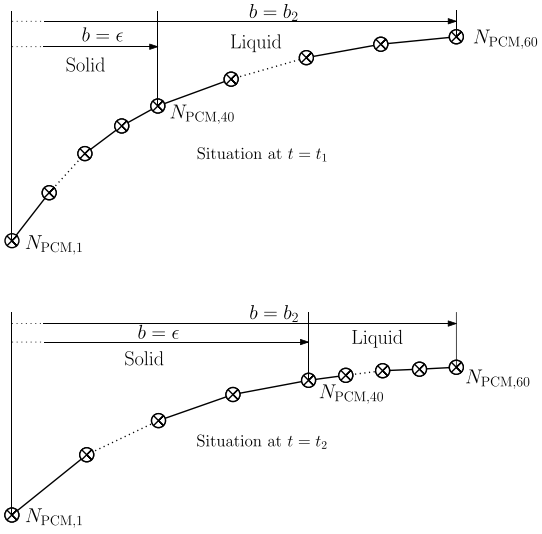

Fig. 3. Scheme of the discretized PCM domain at two different time steps, according to [51].

where $\%wt = \frac{S_c M_{\mathrm{H_2}}}{M_{\mathrm{MH}}}$ is the hydride gravimetric density.

2.3. Numerical solution and model validation

Being $\mathcal{L} \gg b_1$, we discard heat transfer along the z and θ directions and we consider the problem one dimensional along the radial direction. We also assume the problem axi-symmetric by considering only $b > 0$. First, we use a second order central difference scheme method for the spatial discretization and numerical solution of the Eqs. (7), (10) and (11). Then, we use a quasi-constant step size implementation of the Klopfenstein's Numerical Differentiation Formulas [53] of orders 1 to 5 to integrate in time the resulting stiff Differential Algebraic Equations.

We discretize the MH-PCM storage system using $N_t = 150$ nodes, 50 nodes for the MH and 100 nodes for the PCM. Following the variable space network method proposed in [51], the PCM domain is divided in 2 subdomains. The solid region ($b < \epsilon$) is discretized with $N_{\mathrm{PCM},s} = 60$, whose relative distances increase as the solidification front progresses. The liquid region ($b > \epsilon$) is discretized with $N_{\mathrm{PCM},l} = 40$, whose relative distances shrink as the solidification front progresses (see Fig. 3).

To justify our choice on the mesh size, Fig. 4 shows the results of the mesh sensitivity analysis, conducted with 4 different mesh sizes (cases **(a)** to **(d)**) on a canister with $D = 2.5\,\mathrm{cm}$ and $\mathcal{L} = 1.2\,\mathrm{m}$. The ratio between the number of nodes in the MH and in the PCM remains constant for each case, approximately 1:2. Therefore, case **(a)** has 100 nodes in the MH and 200 nodes in the PCM, case **(b)** has 50 nodes in the MH and 100 nodes in the PCM, and so on. Although the hydrogen storage capacity does not present any appreciable shift between coarser and finer meshes, the temperature profile stabilizes at $N_t = 150$, with no appreciable improvement when increasing to $N_t = 300$. Thus, in the following, case **(b)** is selected as working mesh.

The mathematical model here presented is validated with previous experimental research. We simulate the absorption and desorption processes in a reactor with the same geometry, properties, and working conditions presented in [37]. The first experiment, named "small reactor", contains 1 g of $LaNi_5$, is charged at 6 bar and discharged at 0.068 bar. Its external surface temperature is controlled in an oven. The second experiment, named "large reactor", contains 25 g of $LaNi_5$, is charged at 12.7 bar and discharged at 0.086 bar, and uses water as cooling/heating fluid to control the external surface temperature. The time-dependent evolution of the hydrogen storage capacity and the corresponding average reactor temperature are shown in Figs. 5 and 6, respectively. Our numerical results are in good agreement with the averaged data reported in both cases, for both the absorption and desorption processes.

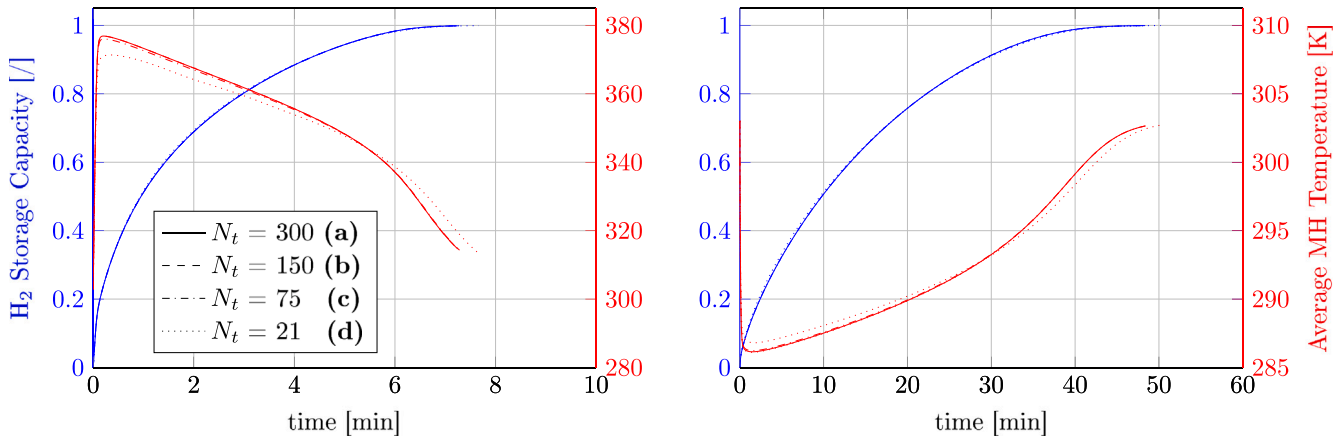

Fig. 4. Mesh sensitivity analysis results in **(left)** absorption and **(right)** desorption. N_t is the total number of nodes along the radius.

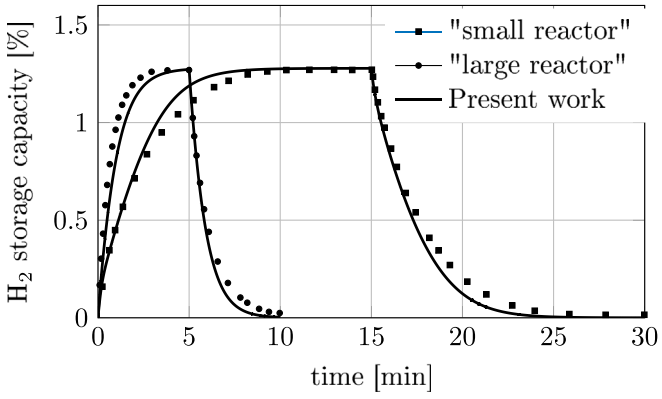

Fig. 5. Validation of the storage capacity profile with [37].

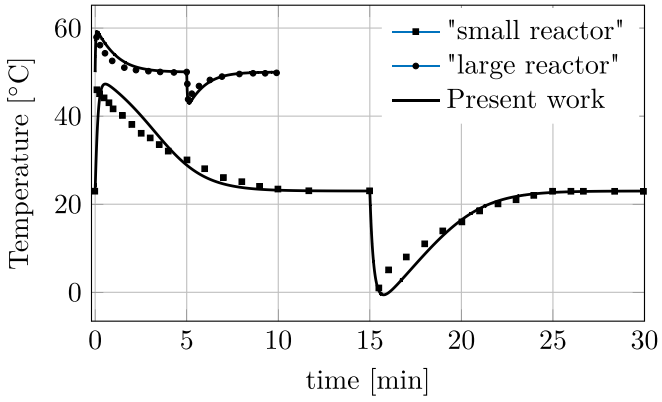

Fig. 6. Validation of reactor temperature profile with [37].

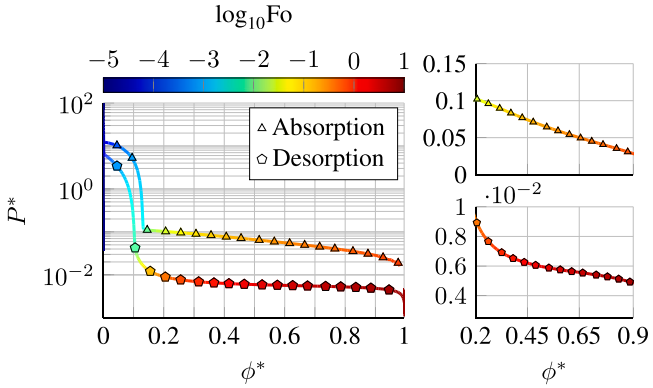

Fig. 7. P^* as a function of ϕ^* in absorption and desorption with Fo in colorbar for the baseline configuration. The correspondent non-dimensional numbers can be seen in Table 1.

2.4. Non-dimensionalization

We represent all the parameters in non-dimensional form, to allow a general analysis of the system performance. Specifically, the 11 non-dimensional parameters represented in Table 1 completely describe the considered phenomena. Π_1 is the non-dimensional equivalent power (P^*). It is directly related to the inlet/outlet hydrogen mass flow rate. A high P^* indicates efficient charge/discharge processes. Π_2 is the Fo number and it suggests the total time needed for the reaction.

To analyze the impact of the system parameters on the absorption/desorption performance (Π_1, Π_2 in non-dimensional form), we separately vary Π_5, Π_6, Π_7, Π_8, Π_9, Π_{10}, Π_{11} within the ranges reported in Table 1. Such ranges are selected to include all feasible configurations (see for instance [19,33,43,54–56]). We add the state-of-charge ϕ to the non-dimensional set of equations. It is equal to 0 when the canister is empty while it is equal to 1 when the canister is fully charged. We use ϕ or, equivalently, $\phi^* = \phi$ for hydrogenation and $1-\phi$ for de-hydrogenation, as progress variable. For each sensitivity analysis we represent Π_1 and Π_2 as functions of ϕ^*. In the following, all results of the sensitivity analysis are compared to a baseline configuration, whose properties are reported in Table 1. Such a configuration is retrieved from [19], where a cylindrical MH-PCM storage system is investigated. Therefore, when considering the varying numbers one at a time, the non-varying parameters are equal to those of the baseline design.

3. Results

Fig. 7 reports P^* as a function of ϕ^* for the baseline case, clearly highlighting 3 different patterns. For $\phi^* < 0.15$ (ϕ_c in the followings) P^* sharply decreases by increasing ϕ^*. This is determined by the reduction of the pressure term in Eqs. (4) and (5). In fact, in this phase, Π_6 is initially much larger than 1 and the heat generated/absorbed by the chemical reaction is significantly higher compared to the thermal power exchanged at the MH-PCM interface (see Fig. 8) and the MH serves as heat reservoir. Therefore, the MH temperature and, consequently, the equilibrium pressure, sharply vary (increasing for absorption and decreasing for desorption). The heat exchange between the MH and the PCM (convection in absorption and conduction in

Table 1
Non-dimensional parameters of the model. (abs) and (des) superscripts indicate absorption and desorption phases. $x = a$ in absorption and d in desorption. $y = 1$ in absorption and -1 in desorption.

	Definition	Baseline value	Range of variation	Denomination
Π_1	$P\frac{D}{\alpha_{MH}^3\rho_{MH}}\frac{1}{10^{18}}$			Equivalent power (P^*)
Π_2	$t\frac{\alpha_{MH}}{D^2}$			Fourier number (Fo)
Π_3	$C_x\frac{D^2}{\alpha_{MH}^2}\frac{1}{10^4}$	$7.5^{(abs)}$ - $1.2^{(des)}$		Kinetic constant
Π_4	$\frac{p_0}{10^5}\frac{D^2}{\alpha_{MH}^2\rho_{MH}}$	$2.5\cdot10^5$		Equilibrium pressure constant
Π_5	$\mathcal{L}/D$	5	[5 , 100]	Main aspect ratio
Π_6	$(p_{env}/p_{eq})^y$	$6^{(abs)}$ - $2.5^{(des)}$	$[6 , 14]^{(abs)}$ $[1.65 , 5]^{(des)}$	Environment pressure
Π_7	$\frac{\mu c_{pPCM}}{k_{PCM}}$	25	[1 , 100]	Prandtl number (Pr)
Π_8	$\lambda\frac{D^2}{\alpha_{PCM}^2}\frac{1}{10^{15}}$	75	[10 , 10^4]	Latent heat of the PCM (λ^*)
Π_9	$\frac{k_{PCM}}{k_{MH}}$	0.1	[0.1 , 0.8]	Thermal conductivities ratio
Π_{10}	$\frac{c_{pPCM}}{c_{pMH}}$	3	[2 , 6]	Specific heats ratio
Π_{11}	$\frac{\rho_{PCM}}{\rho_{MH}}$	0.1	[0.08 , 0.4]	Densities ratio

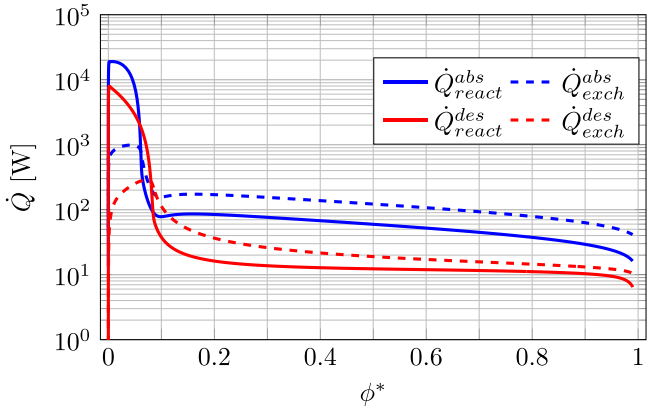

Fig. 8. Reaction power ($\dot{Q}_{react}$) and exchanged thermal power ($\dot{Q}_{exch}$) in absorption and desorption for the baseline design.

desorption) does not impact P^* nor the duration of this phase. Conversely, they are determined by chemical kinetics inside the MH. This first region is characterized by very limited Fo values (Fo < 10^{-3}) and is called *kinetics-limited*. The transition is smoother in desorption and sharper in absorption.

At $\phi^* = \phi_c^*$, the equilibrium pressure nearly equals the inlet/outlet pressure and the reaction rate is significantly and abruptly reduced. Also, the MH temperature reaches the equilibrium temperature.

For $\phi^* > \phi_c^*$, the equilibrium pressure nearly equals the inlet/outlet pressure. Therefore, the reaction rate is significantly reduced and P^* decreases with a quasi-linear behavior as a function of ϕ^* (see Fig. 7). During this stage the thermal power of the hydride reaction is lower than the thermal power exchanged at the interface with the PCM and the MH temperature slowly returns to the initial value. As a consequence, in this phase, heat exchange is the limiting factor that determines P^*. The average slope of the quasi-linear curve in this stage is strictly related to the average MH temperature (i.e., the heat-exchange effectiveness). In particular, when the exchange thermal power is higher (and the average MH temperature is lower), more hydrogen reacts in the same amount of time. This increases the curve slope in the $P^* - \phi^*$ diagram. Note that the heat exchange is significantly slower in desorption than in absorption (see Fig. 8), because, due to the low thermal conductivity of the PCM, conduction is less efficient than convection. Therefore, P^* is higher in absorption than in desorption for every ϕ^*, thanks to the heat being disposed of quickly. In fact, the average absorption power $\overline{P}^*$ is 1.09, whereas in desorption is 0.35. The heat exchange-dominated region is of utmost relevance, since it accounts for the larger portion (between 70% and 80%) of the hydrogen uptake and release. We will focus on finding clues to enhance the heat exchange in this stage, also considering the very brief Fo span of the kinetics-limited region. We can assess the heat exchange efficiency by calculating the average slope $\overline{\frac{\partial P^*}{\partial \phi^*}}$ in this region. In the baseline design, the average slope in absorption is $\overline{\frac{\partial P^*}{\partial \phi^*}} = 0.113$, whereas in desorption is $\overline{\frac{\partial P^*}{\partial \phi^*}} = 0.024$.

As the reacted fraction approaches 1 (i.e., for $\phi^* > 0.95$) the process is again kinetics-limited and the power presents a faster decrease, due to the linear term in Eqs. (4) and (5), that quickly approaches 0, together with r.

3.1. Effect of the canister geometry (Π_5)

Fig. 9.1 shows that, both for absorption and desorption, P^* is directly proportional to $\mathcal{L}/D$ for all values of ϕ^* and that Fo is not a function of $\mathcal{L}/D$ for constant ϕ^*. This means that the time scale of the process remains the same (i.e., at a certain Fo value corresponds the same state of charge). Therefore, by increasing $\mathcal{L}/D$, we increment the system power P^* and the canister absorbs/desorbs more hydrogen per unit time. In fact, longer and thinner canisters exchange heat more efficiently with the PCM, thus increasing P^* in the quasi-linear region. This is due to the higher heat exchange surface-to-volume ratio making the convection/conduction between the MH and the PCM more effective. Also, by increasing $\mathcal{L}/D$, the Rayleigh number increases and, as a consequence, Nu and the convection coefficient h increase, thus enhancing the heat exchange. The regime transition occurs at the same ϕ^* irrespective of $\mathcal{L}/D$, although it is smoother in desorption. This can be explained considering that P^* is not influenced by the heat exchange in the kinetics-limited region. The profiles do not change their average slope of 0.113 in absorption and 0.024 in desorption, thus remaining nearly parallel, while the average power is increased by a factor of 11 in absorption and of 9 in desorption increasing $\mathcal{L}/D$ from 5 to 100. In fact, by increasing $\mathcal{L}/D$ we only scale the system. According to the results, the impact of $\mathcal{L}/D$ is roughly as relevant in absorption as in desorption.

3.2. Effect of hydrogen pressure (Π_6)

Both in absorption and desorption, P^* increases and Fo decreases by increasing Π_6 (i.e., a higher inlet hydrogen pressure or a lower outlet pressure p_{env}), for all the ϕ^* values (Fig. 9.2). The reduction of Fo means that the reaction is effectively quicker when the pressure ratio between the canister and the environment is higher. By increasing the input pressure or decreasing the outlet pressure, the term σ in Eq. (3) increases and so does the hydrogen mass flow rate. This heightens P^* while $\overline{P^*}$ is increased by a factor of 8 in absorption and of 2.5 in desorption varying Π_6 as shown in Fig. 9.2. The transition from the kinetics limited region to the heat exchange-dominated region occurs at different ϕ^* (i.e., ϕ_c^* increases with Π_6). In fact, while the heat diffusion velocity does not change, the reaction's kinetics increases and more hydrogen reacts before reaching ϕ_c^*. Nonetheless, the profiles remain nearly parallel, thus confirming that the heat exchange is not affected by Π_6.

3.3. Effect of Pr (Π_7)

In absorption, the Pr number moderately impacts the system performance (see Fig. 9.3) and ϕ_c^* is not a function of Pr. In fact, for $\phi^* < \phi_c^*$ the PCM does not affect the reaction, because the heat transfer rate towards the PCM is much lower than the thermal power generated in the MH. Conversely, in the heat exchange-dominated region, increasing Pr slightly reduces P^* and Fo due the corresponding reduction of the PCM thermal diffusivity. The average slope of the profiles increases by a factor of 3 by reducing Pr from 100 to 1. This can be explained considering that the same amount of energy is absorbed in less time (i.e., Fo is lower), so that the profile slope is higher at lower Pr numbers. Pr does not impact the desorption phase, because it is only defined for fluids, whereas the PCM is solid during the hydrogen discharge process.

3.4. Effect of latent heat of solidification (Π_8)

In desorption, λ^* does not impact ϕ_c^*, and P^* is not a function of it when $\phi^* < \phi_c^*$. Conversely, for $\phi^* > \phi_c^*$, P^* increases by increasing λ^* (see Fig. 9.3). In fact, incrementing the latent heat of solidification implies a slower evolution of the solidification front and, thus, a more efficient conductive heat exchange. Consequently, varying λ^* from 10 to 10^4 increases $\overline{P^*}$ by a factor of 3. Fo is a function of λ^* as well, suggesting that the time of desorption is significantly reduced for $\lambda^* > 5 \cdot 10^3$. The transition to the heat exchange-dominated region is sharper for higher λ^* and occurs at higher P^*, due to the more effective heat diffusion, as the hydride temperature rises. Notably, the impact of λ^* is more relevant at lower ϕ^* (i.e., close to ϕ_c^*) while the P^* patterns get closer for larger ϕ^*. In fact, towards the end of the process, the relative variation of the solid PCM layer thickness is lower. While λ^* does not affect the absorption power, the system weight reduces with λ^* due to the reduction of PCM mass. This is particularly important when the gravimetric density of the storage system is a predominant factor, like in the automotive sector.

3.5. Effect of thermal conductivity (Π_9)

In Fig. 9.4 we can see that Π_9 significantly impacts the system power for $\phi^* > \phi_c^*$. In this range, a higher Π_9 yields a higher P^* because the PCM absorbs or releases the reaction heat more efficiently. The impact is particularly relevant in desorption, where $\overline{P^*}$ increases by a factor of 4, considering the range of variation of Π_9 shown in Fig. 9.4. Despite the leading heat exchange mechanism in absorption being convection, the increase in relative PCM conductivity helps diffusing the heat from the MH to the PCM and increases the Nu number. The absorption/desorption process requires less time (the reduction of Fo is relevant, in particular for discharge). The curves overlap for $\phi^* < \phi_c^*$ and the transition from the kinetics-limited to the heat exchange-dominated region occurs at the same ϕ^* but it is sharper at higher Π_9. This is particularly evident in desorption, where the average slope increases by a factor of 35 by increasing Π_9 from 0.1 to 0.8.

3.6. Effect of specific heat (Π_{10})

Fig. 9.5 shows that a higher Π_{10} has a slightly positive effect in absorption and a slightly negative effect in desorption. This is due to the different nature of the heat exchange: by increasing the relative PCM specific heat, its relative thermal diffusivity reduces, thus impairing the conductive heat exchange during the discharge phase. Conversely, the convection is enhanced due to the increase of the Ra number. Notably, ϕ_c^* is not a function of Π_{10} nor is the Fo number, confirming that the heat exchange does not impact the kinetics-limited region and that the time required for the process to take place does not change significantly. In desorption, the impact is negligible. In absorption, $\overline{\frac{\partial P^*}{\partial \phi^*}}$ slightly increases by a factor of 2 when increasing Π_{10} from 2 to 6.

3.7. Effect of density (Π_{11})

Finally, Fig. 9.6 shows that Π_{11} has a limited impact on P^*. During absorption, Ra $\propto \frac{\rho_{PCM}}{\rho_{MH}}$ and the heat exchange is positively affected. During desorption, the thermal diffusivity of the PCM is hindered by increasing its density and this impairs the heat exchange efficiency. Neither ϕ_c^* nor Fo are functions of Π_{11}. Therefore, the time required for the reactions remains roughly the same and the behavior of the profiles confirm that the reaction is not influenced by the heat exchange for $\phi^* < \phi_c^*$. Although Π_{11} does not have a significant impact on P^*, a more lightweight PCM increases the system gravimetric density, so lower values of Π_{11} are to be preferred.

4. Discussion

According to Section 3 we observe that Π_5 ($\mathcal{L}/D$) and Π_9 (k_{PCM}/k_{MH}) have the most relevant impact on the absorption and desorption processes. Thus, to optimize the MH-PCM system operation we should use thin and long canisters, surrounded by a PCM with a high value of the relative thermal conductivity. The efficiency of the processes is enhanced thanks to a better heat exchange between MH and PCM, which increases the reaction rate and the inlet/outlet hydrogen mass flow rate. Π_6 and Π_8 play an important role as well. However, Π_6 is mostly dependent on the operational conditions (especially during the discharge phase). Moreover, we note that the latent heat of solidification of the PCM has a primary role only on the desorption efficiency. On the other hand, Pr, Π_{10} (c_{pPCM}/c_{pMH}) and Π_{11} (ρ_{PCM}/ρ_{MH}) have a minor impact on the physical phenomena. Finally, the reactions are limited by the heat exchange with the PCM only for $\phi^* > 0.15$. During the relatively short initial period, the heat exchange non-dimensional parameters do not impact the operation and the different P^* curves overlap. In fact, the MH temperature is still too low (in absorption) or too high (in desorption) to limit the reaction rate. Thus, in this phase, the power (i.e., the hydrogen mass flow rate) is only a function of the reactions kinetics. The same can be observed for the final stage of the reactions (the last 5%), where the kinetics is predominant. Conversely, for $\phi_c^* < \phi^* < 0.95$, the absorption and desorption processes are limited by the heat exchange effectiveness with the surrounding PCM. In this stage, the slope of the P^* patterns is dominated by the heat exchange rate. Therefore, varying the parameters which influence the heat exchange rate yields a variation of the profile slope. Namely, Π_8 and Π_9 are the most relevant numbers in these regards, due to their influence on the profiles slope. Conversely, Π_5, despite notably increasing the average P^*, does not influence the heat exchange effectiveness, because it only changes the storage system scale.

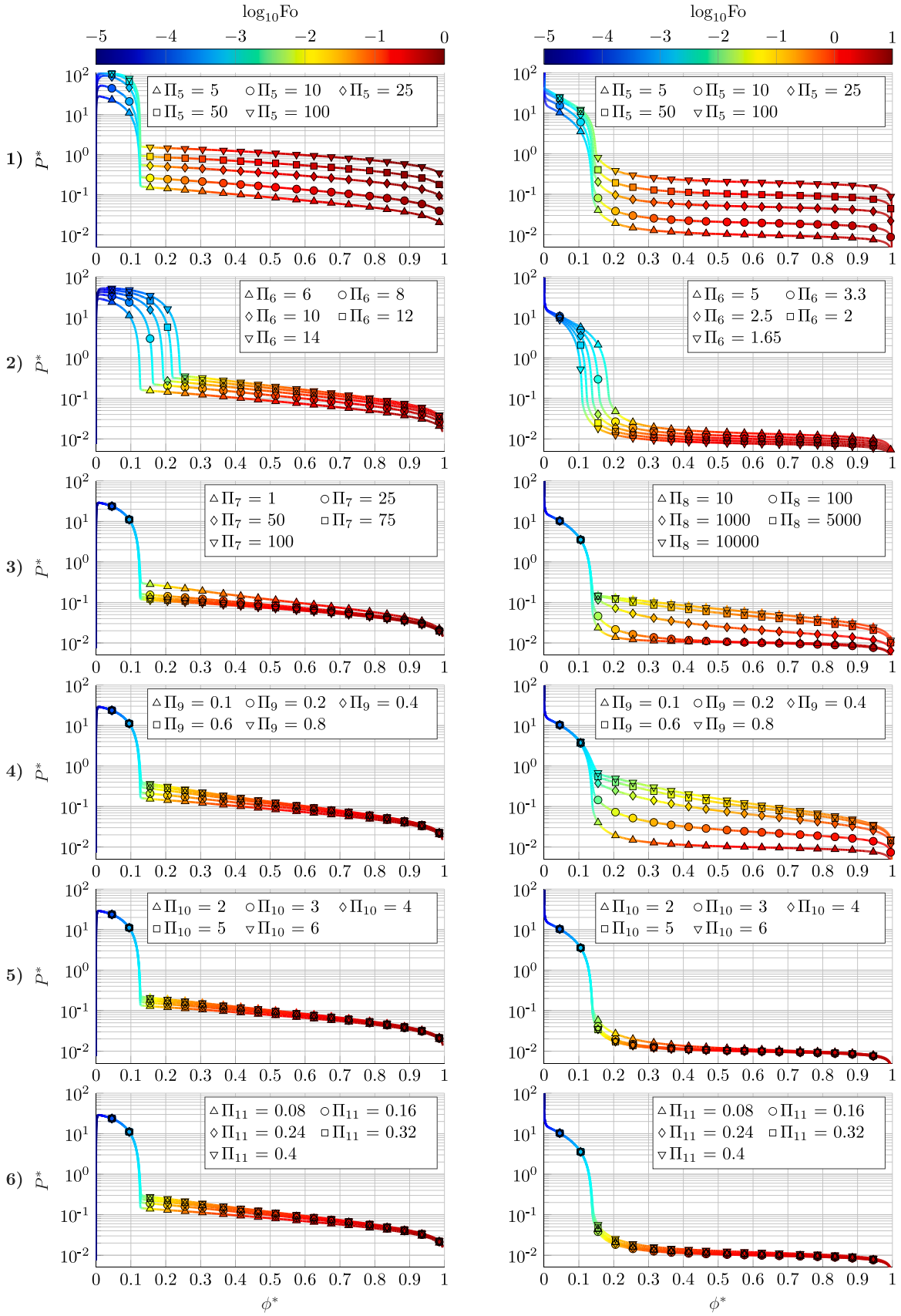

Fig. 9. P^* in absorption (left) and desorption (right) as function of $\mathcal{L}/D$ (1), pressure (2), Pr and λ^* (3), Π_9 (4), Π_{10} (5), and Π_{11} (6), with Fo in colorbar. The non-varying non-dimensional numbers are shown in Table 1.

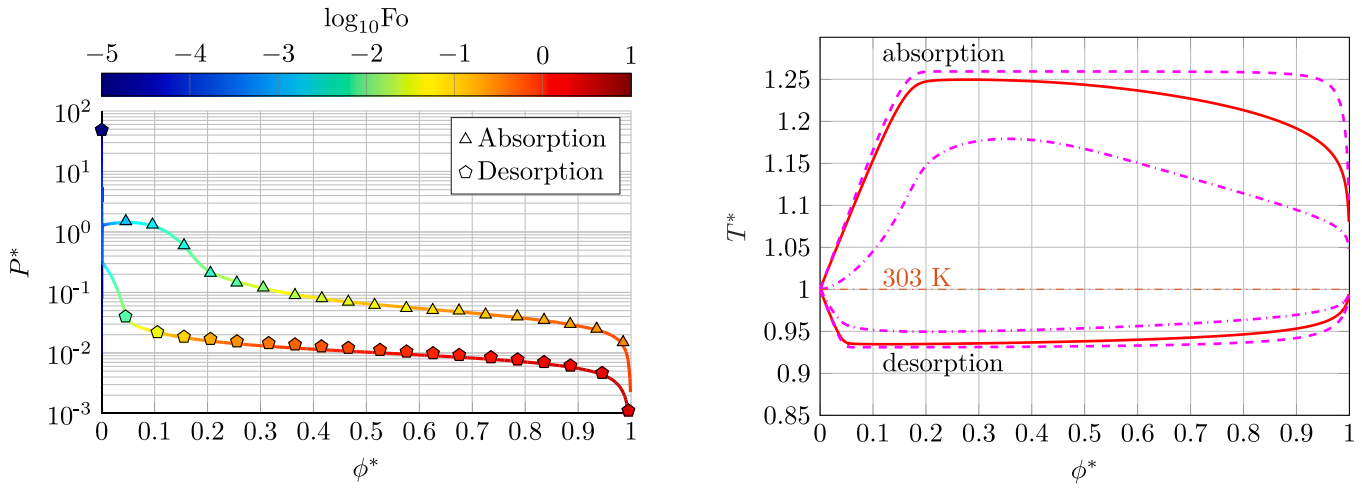

Fig. 10. (left) P^* as a function of ϕ^* with Fo in colorbar and **(right)** temperature profile for Case A. — Reactor average temperature; - - Reactor center; - · MH-PCM interface.

Table 2
Thermo-physical properties of $LiNO_3 - 3H_2O$ according to [33].

Phase change material	$LiNO_3 - 3H_2O$	
Phase	liquid	solid
Thermal conductivity k [W/(m K)]	0.58	1.32
Density ρ [kg/m^3]	1,780	2,140
Specific heat c_p [J/(kg K)]	2,770	1,730
Latent heat of fusion λ [kJ/kg]	296	
Solidification temperature T_{sol} [K]	303	

Ultimately, we comment that the P^* slope in inversely proportional to $\overline{P^*}$. In fact, lower $\overline{P^*}$ corresponds to lower slopes, thus suggesting that a nearly constant power profile throughout the process can only be sustained at relatively low average power values. This becomes especially evident when observing Figs. 9.3 and 9.4.

4.1. Case study A

The goal of this section is to leverage the proposed methodology to design a cylindrical MH-PCM hydrogen storage system. Specifically we seek for a module with a storage capacity of 1 kWh of H_2, that corresponds to 30 g of H_2. To this aim, we select $LaNi_5$ that is one of the most common MHs for similar applications [19]. The PCM will be defined as one of the outcomes of the optimization procedure. The $LaNi_5$ gravimetric density is 1.39% (with $S_c = 3.0$, $M_{MH} = 0.432$ kg/mol, and $M_{H_2} = 0.002$ kg/mol). Therefore 2.16 kg of MH powder are needed and the canister volume is 5.95×10^{-4} m^3. We select a canister with $\Pi_5 = 50$, being $\mathcal{L} = 123.7$ cm and $D = 2.48$ cm. We select a 1" or 2.54 cm diameter for practicality, adjusting the length to 127 cm. The hydrogen stored is therefore equal to 32.4 g, equivalent to 1.08 kWh. We select the PCM to optimize the other controllable parameters (Π_6, Π_7, Π_8, Π_9, Π_{10}, Π_{11}) and we identify $LiNO_3 - 3H_2O$ as best option (see Table 2 for PCM properties and Table 4 for system parameters).

Compared to the baseline design (cfr. Section 2.4), the improved design exhibits a lower charge and discharge power in a first brief phase, then it is more performing (see Fig. 10). Moreover, in both phases the final value of Fo for the improved configuration is notably reduced, thus suggesting a considerably quicker charge and discharge process.

Fig. 10 also shows the non-dimensional temperature $T^* = T/T_{PCM}$ profile for Case A. In dimensional terms, we comment that the temperature range is 12 °C–106 °C. In absorption, there is an evidently heterogeneous distribution of the temperature inside the MH domain, with the center being much hotter (and thus slower) than the PCM interface. Conversely, in desorption the temperature is much more homogeneously distributed, thus indicating a significantly slower reaction.

Fig. 11 shows the charge and discharge power as function of ϕ^* for the baseline and the improved configurations. In absorption, the total time needed for the reaction decreases from 120 min to 12 min, with the correspondent average power increasing from 517.3 W to 5.65 kW. In desorption, the time decreases from 1100 min to 73 min, with the average power increasing from 55.7 W to 830.4 W. Note that, if the same hydride were to exchange heat with air at 293 K, absorption and desorption of 1 kWh of hydrogen would take 1708 min and 1580 min respectively. The average abs/des powers would be 36.3 W and 41.8 W. Ben Mâad et al. [46] have investigated the impact of the PCM's conductivity, melting point, and latent heat in a passively controlled $LaNi_5/LiNO_3$ - $3H_2O$ reactor, while maintaining geometry and other parameters constant. The authors find that increasing the PCM thermal conductivity above 5 W/mK has no significant impact on the reactor performance. They also conclude that decreasing the absorption time to conveniently low values requires a good choice of such three properties. By analyzing the impact of the three above-mentioned parameters, the authors manage to improve the design up to 0.25 kW absorption power and 18 kg_{H_2}/m^3 energy density. By comprehensively investigating the behavior of the storage system, we obtained a higher performance reactor with the same MH and PCM.

We use the exact same amount of PCM that is needed to store/transfer the heat released/required during the entire cycle (1.66 kg). Therefore, such recommended MH-PCM configuration has a 23.01 kg_{H_2}/m^3 density, that is equivalent to a 285 bar pressure vessel at standard temperature. For comparison, the baseline design has a 8 kg_{H_2}/m^3 volumetric density. The MH-air storage system has a 45.3 kg_{H_2}/m^3 volume density, thanks to the more compact design.

4.2. Case studies B and C

Mg_2NiH_4 is now considered as MH. Its properties are reported in Table 3. The reaction enthalpy and activation energy is notably higher than $LaNi_5$. Thus, much more heat is developed/needed for the absorption and desorption processes. Moreover, the equilibrium temperature is consistently much higher. As for case study A, we want to improve a 1 kWh-worth canister with respect to the same baseline design. By employing Mg_2Ni, a High Temperature PCM is needed (HTP). Kenisarin [54] provides a comprehensive review of HTP's. For our application, $NaNO_3$ ($T_{PCM} = 580$ K) and KNO_3 ($T_{PCM} = 608$ K) are the better options. Table 4 reports the recommended configurations for case study B (Mg_2NiH_4 - $NaNO_3$) and case study C (Mg_2NiH_4 - KNO_3). Π_3 and Π_4 change as an unavoidable consequence of employing

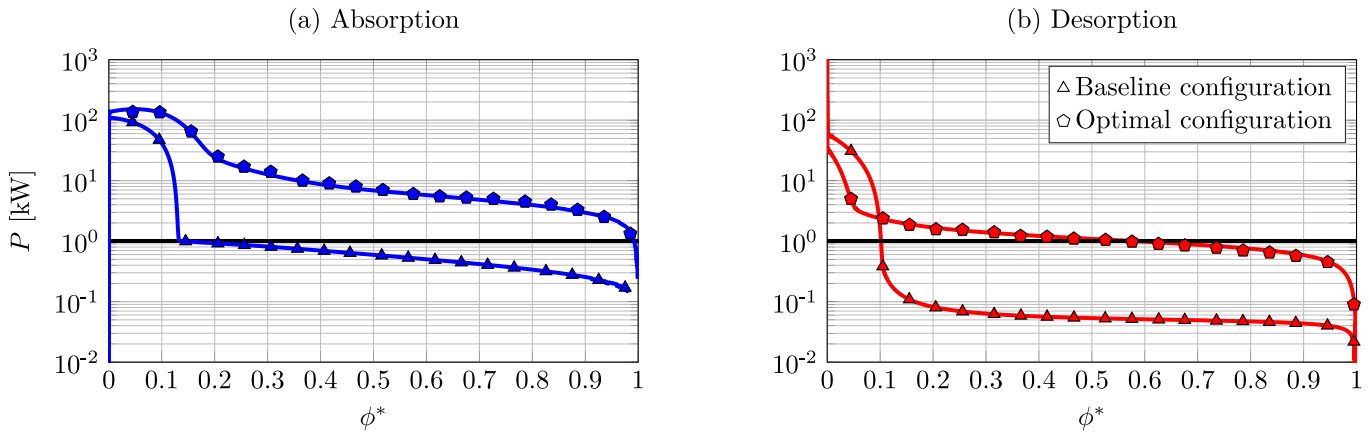

Fig. 11. Comparison between the baseline and the improved configuration of Case A for the (a) Absorption phase and the (b) Desorption phase.

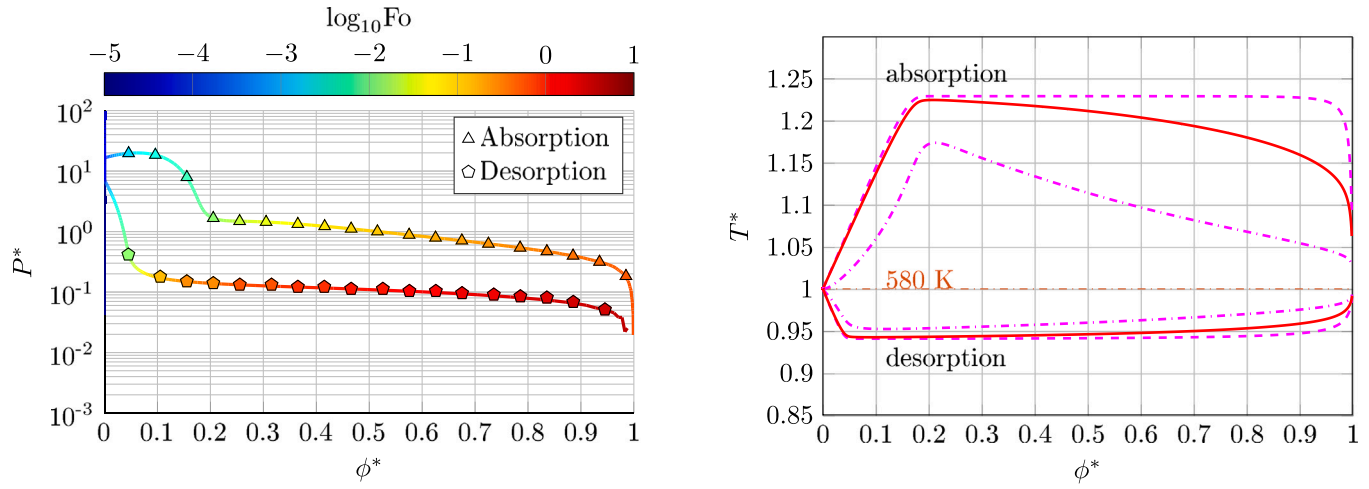

Fig. 12. (left) P^* as a function of ϕ^* with Fo in colorbar and **(right)** temperature profile for Case B. — Reactor average temperature; - - Reactor center; - · MH-PCM interface.

Table 3
Properties of Mg_2NiH_4 MH from [57,58].

Parameter	Value
C_a	175.07 s^{-1}
C_d	5,452.3 s^{-1}
E_a	49,674 J mol^{-1}
E_d	63,468 J mol^{-1}
ΔH_a	−63,336 J mol^{-1}
ΔH_d	68,800 J mol^{-1}
ΔS_a	−120.84 J $mol^{-1}K^{-1}$
ΔS_d	125.6 J $mol^{-1}K^{-1}$
ϵ	0.5
k	0.5 W $m^{-1}K^{-1}$
ρ	2200 kg m^{-3}
c_p	1500 J $kg^{-1}K^{-1}$

a different metal hydride. The table also summarizes the performance of the two layouts.

Figs. 12 and 13 show the non-dimensional power of case study B and case study C, in absorption and desorption. The figures also show the corresponding temperature profiles. We comment that, despite the higher theoretical hydrogen storage capacity of Mg_2NiH_4 (3.73%), $LaNi_5$ exhibits a greater performance, due to the notably greater density of the PCMs employed in case studies B and C.

When we compare case B and C with previous research on the Mg_2Ni hydride, we see how the novel methodology can help in designing a MH-PCM system. Case B and C absorption powers are nearly 4 and 2.5 times higher than the novel multi-zone storage system introduced by Eisapour et al. [59], which exhibits an estimated absorption power of 0.63 kW. In that case, the authors employed air as heat exchange fluid and Mg_2NiH_4 as MH. The volumetric density is impaired (9 kg_{H_2}/m^3 for case B of the present work and 29 kg_{H_2}/m^3 for Eisapour et al.) but we comment that the energy density of case A (23 kg_{H_2}/m^3) is not dramatically lower than that. The comparison shows that a PCM-based passive heat management system can effectively assist controlling the MH temperature and that low-density MH's can be more effective than high-density ones in specific circumstances. The comparison with the work of Chunga and Lin [58] also confirms that MH-PCM systems can be more effective than forced-convection air-based systems at the expense of the volume density. In fact, the authors study an improved configuration of <0.2 kW average desorption power but with a volume density of 49 kg_{H_2}/m^3. The investigated canister is equipped with a central air pipe and with internal fins to increase the heat exchange coefficient and surface, respectively.

5. Conclusions

In this paper we develop a flexible non-dimensional methodology to outline the operation of different cylindrical MH-PCM storage tank layouts and to determine the recommended configuration, in terms of charge/discharge time and equivalent power. We reduce the number of parameters which describe the physical phenomenon by employing 11 non-dimensional numbers. We use such methodology to assess the impact of the relevant geometrical and thermo-physical parameters

Table 4
Summary of the case studies.

Case A	Π_3	Π_4	Π_5	Π_6	Π_7	Π_8	Π_9	Π_{10}	Π_{11}	t [min]	$\overline{P}$ [kW]	wt [%]	ρ_v [kg_{H_2}/m^3]
abs	7.5	2.5×10^5	50	12	4.5	//	0.3	6.5	0.25	12	5.65	0.75	23
des	1.2	2.5×10^5	50	2.5	//	2.5	0.6	4	0.3	73	0.83		
Case B													
abs	1×10^8	2×10^6	30	12	8	//	0.46	1.06	0.63	26	2.33	0.46	8.82
des	4×10^9	2×10^6	30	2.5	//	1.5	0.46	1.06	0.63	205	0.30		
Case C													
abs	1×10^8	2×10^6	30	12	15	//	0.42	1.06	0.59	37	1.66	0.24	6.08
des	4×10^9	2×10^6	30	2.5	//	0.75	0.42	1.06	0.59	110	0.56		

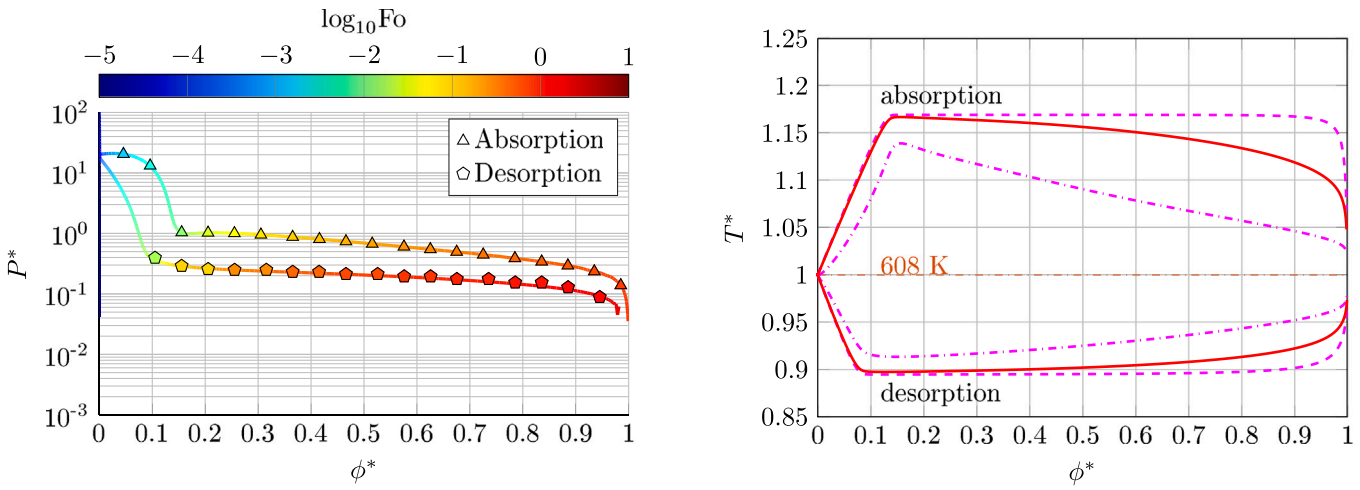

Fig. 13. (left) P^* as a function of ϕ^* with Fo in colorbar and **(right)** temperature profile for Case C. — Reactor average temperature; - - Reactor center; - · MH-PCM interface.

on a baseline design MH-PCM system [19]. Then we evaluate and characterize the recommended configuration. This allows to analyze the performance of the storage system through reduced (11 instead of 16) non-dimensional parameters, with clear advantages in terms of required analysis time and ease of results representation. Such a methodology can be exploited to assess the impact of the most relevant thermo-physical and geometrical factors and, also, to guide the design of the storage system. In fact, when starting the designing process of a MH-PCM hydrogen storage system, a limited set of input parameters are normally given. They can be, typically, the energy storage capacity and the MH material, e.g. 1 kWh and $LaNi_5$. By employing the novel methodology hereby introduced, the output parameters are: the diameter and length of the MH cylinder; the diameter of the outer cylinder (i.e., the PCM radius); the selection of the PCM material; the inlet/outlet power curves, which provide essential information about the dynamic behavior of the storage system; the charge/discharge time; the volumetric and gravimetric energy density. These are selected by investigating the results of the sensitivity analysis presented in Section 3 to find an efficient configuration which stores the given amount of energy and respects possible given constraints (e.g., total volume, and working temperature).

According to the results, the main aspect ratio of the canister ($\mathcal{L}/D$) and the PCM relative thermal conductivity (k_{PCM}/k_{MH}) are the dominant parameters. In fact, we observe that thin and long canisters are more efficient at exchanging heat. Similarly, a high PCM relative thermal conductivity has a significant impact on the desorption process. The non-dimensional latent heat of fusion of the PCM (λ^*) follows as one of the most important parameters, although it only has an impact on the discharge phase. Finally, by starting from the baseline design, we evaluate 3 different cases and propose the recommended configuration, which is designed by analyzing the impact of each of the non-dimensional parameters. A $LaNi_5/LiNO_3 - 3H_2O$ system (case A) for the storage of 1.08 kWh of H_2 exhibits 5.65 kW and 0.83 kW of average power in absorption and desorption, respectively. If compared with the baseline design, the recommended configuration is 93% faster in a charge/discharge cycle, since the total process time is reduced from 1220 min to 85 min.

For what concerns further possible applications, in our vision we are working in the following directions: (i) insert the recommended configuration in a more complex and wide environment (e.g., a multi-energy system), (ii) repeat the analysis for different shapes and geometries (e.g., the spherical geometry), (iii) extend and complete the analysis by using an enhanced PCM with carbon nanoparticles or metal foams and by adding densification in the mathematical model.

CRediT authorship contribution statement

Marco Maggini: Writing – original draft, Visualization, Software, Methodology, Investigation. **Giacomo Falcucci:** Writing – review & editing, Writing – original draft, Project administration, Funding acquisition, Conceptualization. **Alessandro Rosati:** Writing – original draft. **Stefano Ubertini:** Writing – review & editing, Project administration, Funding acquisition. **Andrea L. Facci:** Writing – review & editing, Writing – original draft, Project administration, Methodology, Investigation, Funding acquisition, Conceptualization.

Declaration of competing interest

The authors declare that they have no known competing financial interests or personal relationships that could have appeared to influence the work reported in this paper.

Data availability

All generated data and software used to generate the plots are available at https://github.com/marco-maggini/Paper-Metal-Hydride-non-dimensional-Analysis---Main-Code.git.

Acknowledgments

This project has been partially supported by the projects PRIN P20223JMB3 - Modeling and optimization of sustainable hydrogen refueling infrastructures (HyREFI) and PRIN 2020BFX8JY - Hybrid Sustainable Mobility (HYSUM).

This research was funded by the project ECS 0000024 Rome Technopole, CUP B83C22002820006, National Recovery and Resilience Plan (NRRP) Mission 4 Component 2 Investment 1.5, funded by the European Union-NextGenerationEU.

References

[1] European Commission, A Clean Planet for all - A European strategic long-term vision for a prosperous, modern, competitive and climate neutral economy, 2018, https://eur-lex.europa.eu/legal-content/EN/TXT/PDF/?uri=CELEX:52018DC0773&from=EN. (Accessed 23 May 2022).
[2] United Nations - Department of Economic and Social Affairs, The 17 goals, 2015, https://sdgs.un.org/goals. (Accessed 23 May 2022).
[3] J. Li, J. Fang, Q. Zeng, Z. Chen, Optimal operation of the integrated electrical and heating systems to accommodate the intermittent renewable sources, Appl. Energy 167 (2016) 244–254.
[4] Y. Wu, T. Zhang, R. Gao, C. Wu, Portfolio planning of renewable energy with energy storage technologies for different applications from electricity grid, Appl. Energy 287 (2021) 116562.
[5] R. Bayindir, I. Colak, G. Fulli, K. Demirtas, Smart grid technologies and applications, Renew. Sustain. Energy Rev. 66 (2016) 499–516.
[6] A. Rosati, A.L. Facci, S. Ubertini, Techno-economic analysis of battery electricity storage towards self-sufficient buildings, Energy Convers. Manage. 256 (2022) 115313.
[7] M.A. Rosen, S. Koohi-Fayegh, The prospects for hydrogen as an energy carrier: an overview of hydrogen energy and hydrogen energy systems, Energy Ecol. Environ. 1 (1) (2016) 10–29.
[8] F. Zhang, P. Zhao, M. Niu, J. Maddy, The survey of key technologies in hydrogen energy storage, Int. J. Hydrog. Energy 41 (33) (2016) 14535–14552.
[9] A.L. Facci, D. Sánchez, E. Jannelli, S. Ubertini, Trigenerative micro compressed air energy storage: Concept and thermodynamic assessment, Appl. Energy 158 (2015) 243–254.
[10] A.L. Facci, V. Cigolotti, E. Jannelli, S. Ubertini, Technical and economic assessment of a SOFC-based energy system for combined cooling, heating and power, Appl. Energy 192 (2017) 563–574.
[11] A.L. Facci, S. Ubertini, Analysis of a fuel cell combined heat and power plant under realistic smart management scenarios, Appl. Energy 216 (2018) 60–72.
[12] G. Loreti, A.L. Facci, I. Baffo, S. Ubertini, Combined heat, cooling, and power systems based on half effect absorption chillers and polymer electrolyte membrane fuel cells, Appl. Energy 235 (2019) 747–760.
[13] S. Ubertini, A.L. Facci, L. Andreassi, Hybrid hydrogen and mechanical distributed energy storage, Energies 10 (12) (2017) 2035.
[14] L. Zhou, Progress and problems in hydrogen storage methods, Renew. Sustain. Energy Rev. 9 (4) (2005) 395–408.
[15] M. Afzal, N. Sharma, N. Gupta, P. Sharma, Transient simulation studies on a metal hydride based hydrogen storage reactor with longitudinal fins, J. Energy Storage 51 (2022).
[16] Z. Dong, Y. Wangb, H. Wua, X. Zhanga, Y. Suna, Y. Lia, J. Changa, Z. Hea, J. Hong, A design methodology of large-scale metal hydride reactor based on schematization for hydrogen storage, J. Energy Storage 49 (2022).
[17] C. Drawer, J. Lange, M. Kaltschmitt, Metal hydrides for hydrogen storage - identification and evaluation of stationary and transportation applications, J. Energy Storage 77 (2024).
[18] N. Klopčič, I. Grimmer, F. Winkler, M. Sartory, A. Trattner, A review on metal hydride materials for hydrogen storage, J. Energy Storage 63 (2023).
[19] A.L. Facci, M. Lauricella, S. Succi, V. Villani, G. Falcucci, Optimized modeling and design of a PCM-enhanced H2 storage, Energies 14 (6) (2021) 1554.
[20] S. Jana, P. Muthukumar, Design, development and hydrogen storage performance testing of a tube bundle metal hydride reactor, J. Energy Storage 63 (2023).
[21] S.D. Lewis, P. Chippar, Analysis of heat and mass transfer during charging and discharging in a metal hydride-phase change material reactor, J. Energy Storage 33 (2021) 102108.
[22] E.I. Gkanas, M. Khzouz, G. Panagakos, T. Statheros, G. Mihalakakou, G.I. Siasos, G. Skodras, S.S. Makridis, Hydrogenation behavior in rectangular metal hydride tanks under effective heat management processes for green building applications, Energy 142 (2018) 518–530.
[23] L. Tong, J. Xiao, T. Yang, P. Bénard, R. Chahine, Complete and reduced models for metal hydride reactor with coiled-tube heat exchanger, Int. J. Hydrog. Energy 44 (30) (2019) 15907–15916.
[24] C.A. Krokos, D. Nikolic, E.S. Kikkinides, M.C. Georgiadis, A.K. Stubos, Modeling and optimization of multi-tubular metal hydride beds for efficient hydrogen storage, Int. J. Hydrog. Energy 34 (22) (2009) 9128–9140.
[25] F. Askri, M.B. Salah, A. Jemni, S.B. Nasrallah, Optimization of hydrogen storage in metal-hydride tanks, Int. J. Hydrog. Energy 34 (2) (2009) 897–905.
[26] C. Veerraju, M.R. Gopal, Heat and mass transfer studies on plate fin-and-elliptical tube type metal hydride reactors, Appl. Therm. Eng. 30 (6–7) (2010) 673–682.
[27] C. Chung, S.-W. Yang, C.-Y. Yang, C.-W. Hsu, P.-Y. Chiu, Experimental study on the hydrogen charge and discharge rates of metal hydride tanks using heat pipes to enhance heat transfer, Appl. Energy 103 (2013) 581–587.
[28] B.M. Diaconu, M. Cruceru, L. Anghelescu, A critical review on heat transfer enhancement techniques in latent heat storage systems based on phase change materials. Passive and active techniques, system designs and optimization, J. Energy Storage 61 (2023).
[29] S. Garrier, B. Delhomme, P. De Rango, P. Marty, D. Fruchart, S. Miraglia, A new MgH2 tank concept using a phase-change material to store the heat of reaction, Int. J. Hydrog. Energy 38 (23) (2013) 9766–9771.
[30] A.A.R. Darzi, H.H. Afrouzi, A. Moshfegh, M. Farhadi, Absorption and desorption of hydrogen in long metal hydride tank equipped with phase change material jacket, Int. J. Hydrog. Energy 41 (22) (2016) 9595–9610.
[31] S.N. Nyamsi, I. Tolj, S. Pasupathi, Multi-objective optimization of a metal hydride reactor coupled with phase change materials for fast hydrogen sorption time, J. Energy Storage 71 (2023).
[32] G. Amati, S. Succi, G. Falcucci, Enhancing the power performance of latent heat thermal energy storage systems: The adoption of passive, fractal supports, Energies 16 (2023).
[33] H. El Mghari, J. Huot, L. Tong, J. Xiao, Selection of phase change materials, metal foams and geometries for improving metal hydride performance, Int. J. Hydrog. Energy 45 (29) (2020) 14922–14939.
[34] H.Q. Nguyen, M. Mourshed, B. Paul, B. Shabani, An experimental study of employing organic phase change material for thermal management of metal hydride hydrogen storage, J. Energy Storage 55 (2022).
[35] S. Nyallang Nyamsi, I. Tolj, M. Lototskyy, Metal hydride beds-phase change materials: Dual mode thermal energy storage for medium-high temperature industrial waste heat recovery, Energies 12 (20) (2019) 3949.
[36] D.N. Nkwetta, F. Haghighat, Thermal energy storage with phase change material-A state-of-the art review, Sustain. Cities Soc. 10 (2014) 87–100.
[37] F. Laurencelle, J. Goyette, Simulation of heat transfer in a metal hydride reactor with aluminium foam, Int. J. Hydrog. Energy 32 (14) (2007) 2957–2964.
[38] S. Ferekh, G. Gwak, S. Kyoung, H.-g. Kang, M.-h. Chang, S.-h. Yun, Y.-h. Oh, W. Kim, D. Kim, T. Hong, et al., Numerical comparison of heat-fin-and metal-foam-based hydrogen storage beds during hydrogen charging process, Int. J. Hydrog. Energy 40 (42) (2015) 14540–14550.
[39] C. Wang, T. Lin, N. Li, H. Zheng, Heat transfer enhancement of phase change composite material: Copper foam/paraffin, Renew. Energy 96 (2016) 960–965.
[40] Y. Du, Y. Ding, Towards improving charge/discharge rate of latent heat thermal energy storage (LHTES) by embedding metal foams in phase change materials (PCMs), Chem. Eng. Process.: Process Intensif. 108 (2016) 181–188.
[41] A. Chibani, S. Merouani, C. Bougriou, The performance of hydrogen desorption from a metal hydride with heat supply by a phase change material incorporated in porous media (metal foam): Heat and mass transfer assessment, J. Energy Storage 51 (2022).
[42] J.S. Prasad, P. Muthukumar, Design and performance analysis of an annular metal hydride reactor for large-scale hydrogen storage applications, Renew. Energy 181 (2022).
[43] Y. Ye, J. Ding, W. Wang, J. Yan, The storage performance of metal hydride hydrogen storage tanks with reaction heat recovery by phase change materials, Appl. Energy 299 (2021) 117255.
[44] A. Chaise, P. de Rango, P. Marty, D. Fruchart, Experimental and numerical study of a magnesium hydride tank, Int. J. Hydrog. Energy 35 (12) (2010) 6311–6322.
[45] Z. Bao, F. Yang, Z. Wu, X. Cao, Z. Zhang, Simulation studies on heat and mass transfer in high-temperature magnesium hydride, Appl. Energy 112 (2013) 1181–1189.
[46] H.B. Maad, F. Askri, S.B. Nasrallah, Heat and mass transfer in a metal hydrogen reactor equipped with a phase-change heat-exchanger, Int. J. Therm. Sci. 99 (2016) 271–278.
[47] S. Mellouli, E. Abhilash, F. Askri, S.B. Nasrallah, Integration of thermal energy storage unit in a metal hydride hydrogen storage tank, Appl. Therm. Eng. 102 (2016) 1185–1196.
[48] B. von Colbe, et al., Application of hydrides in hydrogen storage and compression: Achievements, outlook and perspectives, Int. J. Hydrog. Energy 44 (2019).
[49] B. Talagañis, G. Meyer, P. Aguirre, Modeling and simulation of absorption-desorption cyclic processes for hydrogen storage-compression using metal hydrides, Int. J. Hydrog. Energy 36 (2011).
[50] Y. Ye, J. Lu, J. Ding, W. Wang, J. Yan, Numerical simulation on the storage performance of a phase change materials based metal hydride hydrogen storage tank, Appl. Energy 278 (2020) 115682.
[51] W.D. Murray, F. Landis, Numerical and machine solutions of transient heat-conduction problems involving melting or freezing. Part l-Method of analysis and sample solutions, J. Heat Transfer ASME (1959) 106–112.
[52] P. Jany, A. Bejan, Scaling theory of melting with natural convection in an enclosure, Int. J. Heat Mass Transfer 31 (1988).

[53] R.W. Klopfenstein, Numerical differentiation formulas for stiff systems of ordinary differential equations, RCA Rev. 32 (1971).
[54] M.M. Kenisarin, High-temperature phase change materials for thermal energy storage, Renew. Sustain. Energy Rev. 14 (2010).
[55] L. Tong, J. Xiao, P. Bénard, R. Chahine, Thermal management of metal hydride hydrogen storage reservoir using phase change materials, Int. J. Hydrog. Energy 44 (38) (2019) 21055–21066.
[56] S. Mellouli, N.B. Khedher, F. Askri, A. Jemni, S.B. Nasrallah, Numerical analysis of metal hydride tank with phase change material, Appl. Therm. Eng. 90 (2015) 674–682.
[57] Z. Wu, F.S. Yang, Z.W. Bao, S.N. Nyamsi, Y.Q. Wang, Z.X. Zhang, Microstructure and improved hydrogen storage properties of Mg based alloy powders prepared by modified milling method, Powder Metall. 57 (2014).
[58] C. Chunga, C.-S. Lin, Prediction of hydrogen desorption performance of Mg2Ni hydride reactors, Int. J. Hydrog. Energy 34 (2009).
[59] A.H. Eisapour, M. Eisapour, P. Talebizadehsardari, G. Walker, An innovative multi-zone configuration to enhance the charging process of magnesium based metal hydride hydrogen storage tank, J. Energy Storage 36 (2021).